PHYSICAL REVIEW MATERIALS **10**, 035801 (2026)

Exploring the hydrogen evolution reaction performance on a borophene monolayer

Jing Liu [*] and Axel Groß [†]
Institute of Theoretical Chemistry, Ulm University, Mez-Starck-Haus, Oberberghof 7, 89081 Ulm, Germany

(Received 13 October 2025; revised 22 December 2025; accepted 17 February 2026; published 5 March 2026)

Borophene, a unique two-dimensional boron-based material with a graphenelike structure, has attracted growing interest due to its special configurations and remarkable physical and chemical properties. This study focuses on four different borophene phases: α, $\beta12$, $\gamma3$, and trigonal, and systematically investigates their hydrogen evolution reaction (HER) performance. By using density functional theory (DFT), we evaluate the intrinsic catalytic activity of freestanding borophene monolayers as well as the influence of an Ag(111) substrate on their HER behavior. The results indicate that the freestanding α, $\beta12$, and $\gamma3$ phases exhibit excellent HER activity, characterized by optimal Gibbs free energies for hydrogen adsorption. Especially, the on-top site with the lowest coordination number is identified as the most active site. However, interaction with the Ag(111) support significantly modifies the hydrogen binding, leading to suppressed HER performance in these phases. In contrast, the trigonal phase displays relatively poor HER performance, attributed to its fully saturated bonding environment, while the silver substrate significantly modifies its geometric configuration and slightly enhances the HER performance. This work highlights both the promising intrinsic HER potential of borophene monolayers and the critical impact of substrate interactions, guiding the design of efficient borophene-based electrocatalysts.

DOI: 10.1103/kk8v-1b2l

I. INTRODUCTION

Low-dimensional materials have attracted extensive research interest due to their unique physical and chemical properties, which often differ significantly from their bulk counterparts [1–6]. As is well known, carbon already plays an important role in the formation of low-dimensional materials, giving rise to a variety of well-known allotropes across different dimensions, namely zero-dimensional fullerenes [7–10], one-dimensional carbon nanotubes [11–13], and two-dimensional graphene [14–18], each exhibiting distinct electronic and mechanical properties. Graphene has emerged as a prototype 2D material due to its exceptional properties, such as ultrahigh carrier mobility, superior mechanical strength, and excellent thermal conductivity [19–21]. These remarkable properties lead to its widespread applications in nanoelectronics, energy storage, and catalysis [20,22–26]. Given the success of carbon-based materials, it naturally raises the question: Are there other elements, particularly those near carbon in the periodic table, that could form similar low-dimensional structures? Boron, in this regard, stands out as one of the most promising elements. Its unique bonding flexibility allows it to form diverse low-dimensional configurations, such as boron buckyballs [27–30], boron nanotubes [31–33], and boron sheets [34–36].

In particular, the atomically thin 2-D boron sheet, so-called borophene, has first been synthesized on the Ag(111) surface, inspiring a wide interest in investigations on the 2-D boron structures [35,37,38]. For instance, Kiraly *et al.* successfully synthesized and characterized nanoscale borophene on Au(111) in UHV [39]. Li *et al.* reported a graphene-like honeycomb borophene structure grown on an Al(111) surface via molecular beam epitaxy under ultrahigh vacuum conditions [40]. Wu *et al.* successfully grew borophene on Cu(111) surfaces, obtaining large single-crystal domains with sizes up to 100 μm^2 [41]. Recent theoretical studies have also revealed the exfoliation mechanism of borophene, showing that high-density stacking faults in β-rhombohedral boron can significantly lower the exfoliation energy barrier, thus facilitating the formation of boron sheets [42]. This mechanism enhances the understanding of borophene synthesis and, in the meantime, makes borophene more promising for future applications.

Unlike the carbon atom, the unique electronic configuration of boron favors the formation of two-dimensional lattices composed of triangular and hexagonal motifs, leading to a richer variety of structures compared to graphene, including the α, $\beta12$, $\gamma3$ phases, and others [34,43–49]. Previous theoretical studies have shown that most borophene structures exhibit metallic behavior and, in certain structures, display a Dirac feature analogous to that in graphene [35,50,51]. These electronic characteristics, combined with the good carrier mobility, indicate that borophene can serve as an efficient electrode material [52,53]. In addition, several studies have demonstrated the notable electrocatalytic properties of various boron sheets [54–59]. Notably, the development of sustainable energy technologies requires highly efficient electrocatalysts for the hydrogen evolution reaction (HER), which is the key half-reaction for generating hydrogen. Nevertheless, the

---

[*] Contact author: jing-1.liu@uni-ulm.de
[†] Contact author: axel.gross@uni-ulm.de

traditional noble-metal catalysts, such as platinum, are limited by their high cost [60]. The search for cheap alternatives to Pt has led to numerous research efforts [61,62]. Considering the relatively low cost of boron, it exhibits great potential as an alternative for HER.

In this work, we investigate the HER on borophene using first-principles calculations. Four different borophene phases (α, $\beta 12$, $\gamma 3$, and trigonal) are analyzed to determine their catalytic activity, with a focus on optimized structures, potential energy surface, and adsorption energy. Furthermore, the impact of metal substrates on HER performance is also explored, showing that the adsorption behavior on free-standing two-dimensional sheets can be significantly altered when these sheets are supported by a metallic substrate. Our findings provide insights into the potential of borophene-based materials for electrocatalysis.

II. COMPUTATIONAL DETAILS

We conducted first-principles calculations using density functional theory (DFT) as implemented in the Vienna *Ab initio* Simulation Package (VASP) [63,64]. The projector augmented wave (PAW) method was adopted to treat the interaction between valence electrons and ionic cores [65].

Exchange-correlation interactions are described with the revised Perdew-Burke-Ernzerhof (RPBE) functional within the generalized gradient approximation (GGA) together with the D3 dispersion correction with Becke-Johnson damping (D3BJ) to account for long-range van der Waals interactions [66–68]. This combination has been shown to provide an accurate estimate of the adsorption energetics across a wide range of adsorbates and metal surfaces [69]. To ensure computational accuracy and convergence, we employed a plane-wave energy cutoff of 550 eV. A vacuum layer of 20 Å was introduced along the out-of-plane direction (z axis) to eliminate artificial interactions between periodic images in the slab model.

Full structural relaxations are performed until the total energy and atomic forces converge to thresholds of 10^{-4} eV/atom and 0.01 eV/Å, respectively. For Brillouin zone integration, a $5 \times 5 \times 1$ Monkhorst-Pack k-point mesh was used. Based on the optimized structures, we further performed single-point total energy (SPE) calculations with a higher level of precision. A denser $13 \times 13 \times 1$ k-point mesh was adopted to ensure accurate energy evaluation. Notably, for the relatively smaller supercell of the trigonal phase, a k-point mesh of $11 \times 11 \times 1$ was used for structural relaxation, and $19 \times 19 \times 1$ was used for the SPE calculations. Note that the k-point sampling was carefully tested for each borophene phase by varying the k mesh from $3 \times 3 \times 1$ to $21 \times 21 \times 1$ to ensure convergence. For the electronic occupation, the zero-width Gaussian smearing was employed. Dipole corrections were also applied in all slab calculations to properly account for charge redistribution and interfacial dipoles. Zero-point energy (ZPE) and thermal corrections were obtained using the postprocessing package VASPKIT [70], based on finite-difference phonon calculations in VASP. The same $5 \times 5 \times 1$ Monkhorst-Pack k-point grid was used to ensure the accuracy of vibrational frequencies. The thermal contributions to the Gibbs free energy were calculated at 298.15 K.

Under acidic conditions, the overall HER can be expressed as

$$2\mathrm{H}^+ + 2\mathrm{e}^- \rightarrow \mathrm{H}_2. \tag{1}$$

In the Volmer-Heyrovsky mechanism [71], it proceeds through two primary steps, the adsorption of an H atom onto the catalyst surface and a desorption process where another H atom combines with the adsorbed H atom to form molecular hydrogen:

$$\mathrm{H}^+ + \mathrm{e}^- + * \rightarrow \mathrm{H}^* \tag{2}$$

$$\mathrm{H}^+ + \mathrm{e}^- + \mathrm{H}^* \rightarrow \mathrm{H}_2, \tag{3}$$

where $*$ represents an active site and H^* indicates a hydrogen atom adsorbed on the catalyst surface. The structural optimizations and the corresponding ZPE corrections for H-adsorbed borophenes are performed using the same computational parameters and workflow as described above. The free energy of hydrogen adsorption (ΔG_{H}) is widely regarded as a key descriptor for evaluating the catalytic performance of HER [72], which is given by

$$\Delta G_{\mathrm{H}^*} = \Delta E_{\mathrm{H}} + \Delta E_{\mathrm{ZPE}} - T\Delta S_{\mathrm{H}} \tag{4}$$

$$\Delta E_{\mathrm{H}} = E_{n\mathrm{H}^*} - E_{(n-1)\mathrm{H}^*} - \tfrac{1}{2}E_{\mathrm{H}_2}, \tag{5}$$

where ΔE_{H} is the change in electronic energy due to hydrogen adsorption, ΔE_{ZPE} represents the change in zero-point energy, T is the temperature, and ΔS_{H} denotes the change in entropy of the hydrogen atom during adsorption. $E_{n\mathrm{H}^*}$ and E_{H_2} are the electronic energy of the system with n adsorbed H atoms and hydrogen molecule, respectively. We first focused on the freestanding borophene sheets, and subsequently constructed borophene/Ag(111) heterostructures to simulate realistic substrate-supported systems.

III. RESULTS AND DISCUSSION

To establish a comprehensive understanding of the intrinsic properties of borophene, we began our investigation with freestanding monolayer structures, avoiding the influence of external perturbations such as substrates or dopants. It enabled us to examine the fundamental electronic structure and catalytic characteristics of borophene in its freestanding state. In particular, we systematically explored the HER performance by evaluating the hydrogen adsorption behavior at various adsorption sites on four borophene phases: α, β_{12}, γ_3, and trigonal. These structures were chosen based on their distinct bonding motifs and stability profiles as reported in previous studies. Considering that most borophene structures are experimentally synthesized on metallic substrates, we investigated the influence of metal support on their catalytic performance. In this work, an Ag(111) surface was selected as a representative substrate, given its frequent use in the epitaxial growth of borophene. By comparing the energetics and electronic structures of borophene before and after substrate introduction, we systematically evaluated the impact of substrate effects on its catalytic behavior.

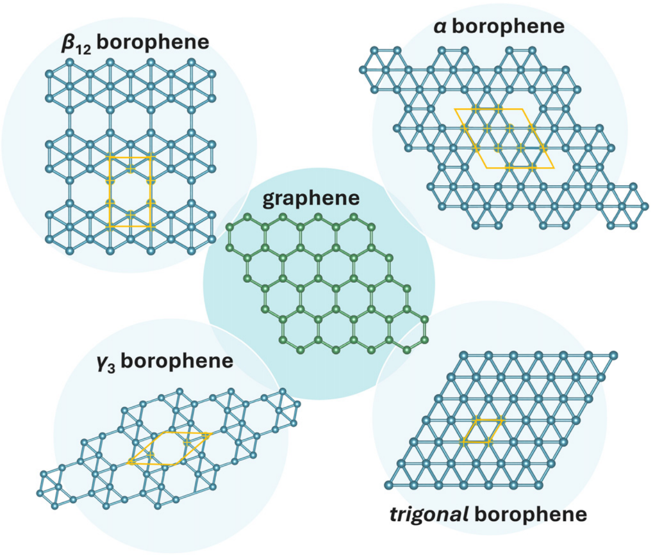

FIG. 1. Geometric configurations of graphene (center panel) and four freestanding borophenes. The structures shown from left to right and top to bottom correspond to the β_{12}, α, γ_3, and trigonal phases, respectively. The primitive unit cell of each phase is highlighted in yellow line.

A. Structure and stability of freestanding surface

Four freestanding borophene surfaces are taken as examples. The trigonal borophene is a two-dimensional planar lattice composed entirely of triangular motifs. α, β_{12}, and γ_3 phases are formed by introducing vacancies at specific positions within the trigonal surface. Compared to the hexagonal lattice of graphene, these borophenes have additional atoms in the centers of the vacant hexagons. Notably, the latter three phases have already been successfully synthesized in experiments [46,47,49]. Figure 1 shows the four borophene configurations. Due to the distinct atomic arrangements, the bonding environments in these four phases differ significantly. For instance, the trigonal phase consists entirely of fully coordinated boron atoms, whereas the α phase additionally contains fivefold coordinated boron atoms due to the presence of vacancies. In contrast, the γ_3 phase includes only five- and fourfold coordinated boron atoms. The β_{12} phase contains all the above bonding types. These bonding variations strongly suggest that also the HER performance of these different phases might be distinct. To model the adsorption configurations and ensure negligible periodic interactions between adsorbates, different sufficiently large supercell sizes were used for each phase: a $2 \times 2 \times 1$ supercell for the α phase, $3 \times 2 \times 1$ for the β_{12} phase, $3 \times 3 \times 1$ for the γ_3 phase, and $3 \times 3 \times 1$ for the trigonal phase. Remarkably, these structural modifications preserve the overall planar geometry of surfaces with respect to perpendicular relaxations. To examine the stability of the planar structure, we applied various arbitrary distortions along the out-of-plane direction. In all scenarios, the systems relaxed back to nearly perfect planar configurations, indicating the intrinsic robustness of the two-dimensional geometry. The lengths of the boron bonds range from 1.63 to 1.75 Å. Detailed information about each lattice is provided in Table I. To evaluate the relative thermodynamic stability of the four borophene phases, we compared their free energy per unit area, $\sigma = E_{\text{borophene}}/A$, where $E_{\text{borophene}}$ is the total free energy of the freestanding borophene and A is the area of boron surface in the supercell. This analysis yields that the trigonal phase exhibits the lowest energy per unit area with the value of -2.443 eV/Å^2. The α phase has a slightly higher energy (-2.338 eV/Å^2). The energy per unit area of the β phase is -2.157 eV/Å^2. The γ_3 phase with a formation energy per unit area of -2.096 eV/Å^2 is the energetically least favorable structure among the considered phases.

TABLE I. Average B–B bond length of the four borophene phases. The notation "bl(m-n)" refers to the length of a B–B bond formed between m-fold coordinated and n-fold coordinated boron atoms. Unit of each value is Å.

Phases	bl(4-4)	bl(4-5)	bl(4-6)	bl(5-5)	bl(5-6)	bl(6-6)
α	—	—	—	1.671	1.687	—
β_{12}	1.644	1.678	1.711	1.753	1.700	—
γ_3	1.611	1.691	—	1.638	—	—
Trigonal	—	—	—	—	—	1.704

B. HER performance of freestanding borophenes

To better understand the interaction between hydrogen and various phases, potential energy surfaces (PES) are first mapped on the monolayer borophene with a single H atom adsorbed. Considering surface symmetry and periodicity, the H atom is moved within a specific region on each surface, which consists of two adjacent triangular units [highlighted in yellow in Fig. 2(a)]. This area includes both high- and low-coordination sites, thereby capturing the essential electronic features of the entire surface. The vertical distance between H and borophene is determined by scanning the total energy as a function of height. The distance corresponding to the minimum energy is chosen and fixed in the subsequent PES evaluations. For α, β_{12}, γ_3, and trigonal phases, the H-borophene distances are fixed as 1.710, 1.712, 1.690, and 1.760 Å, respectively. Note that typically potential energy surfaces are determined with all remaining coordinates fixed [73,74] because only then they are well-defined and reproducible. We evenly selected 100×100 sampling points within the aforementioned surface region. The single-point energy at each sampling point is calculated using the computational parameters mentioned in the previous section (the boron atoms are frozen here). The lowest energy of each phase is taken as the reference. The resulting PES maps are shown in Figs. 2(b)–2(e). It reveals that areas near lower-coordinated on-top adsorption sites exhibit lower potential energy, such as the fivefold site on α, the fourfold site on both β_{12} and γ_3. Notably, for the trigonal phase, composed entirely of saturated boron atoms, all on-top sites show identical potential energies that are lower than those at other adsorption sites, such as bridge and hollow sites. This suggests that hydrogen atoms preferentially adsorb at undercoordinated boron sites, where stronger interactions are expected.

Here, the HER mechanism is described by the Volmer-Heyrovsky pathway, as shown in Eqs. (2) and (3). Combined with the PES results and geometric features of the four

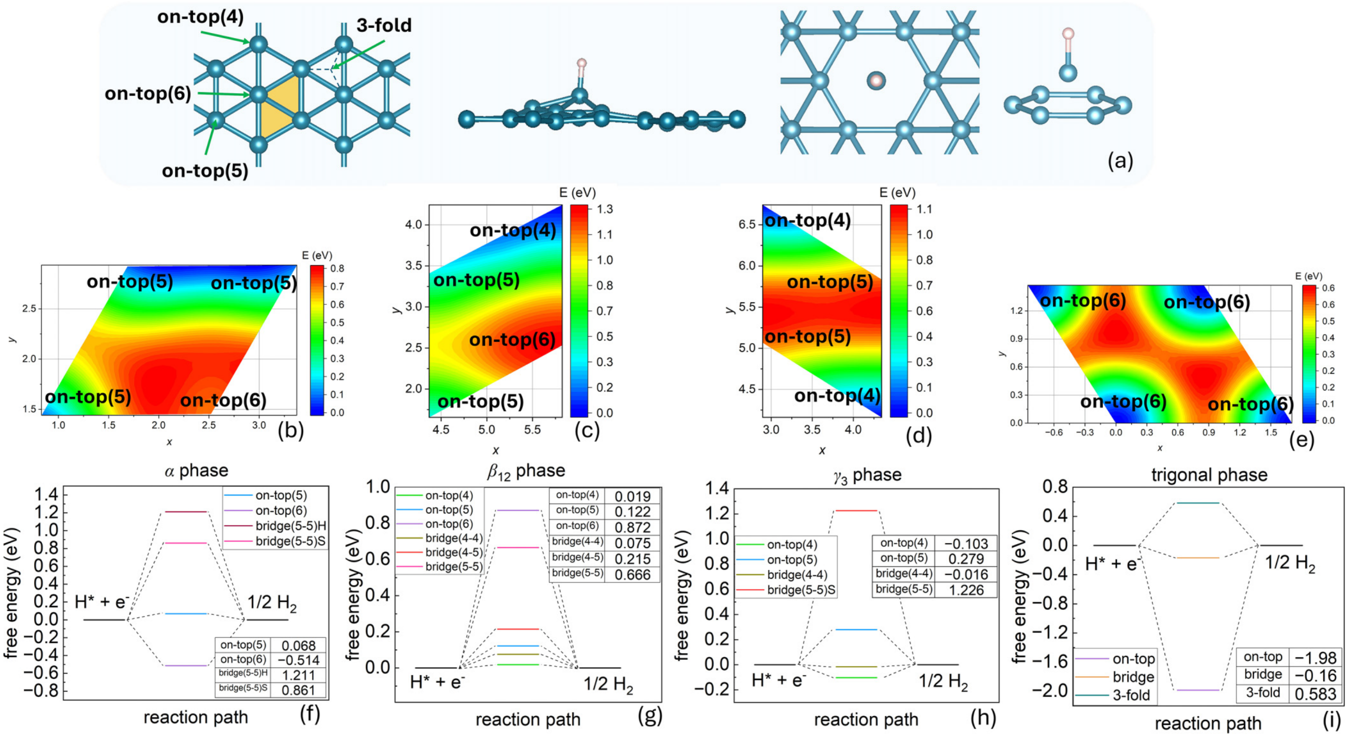

(f)	ΔG_{H^*}
on-top(5)	0.068
on-top(6)	−0.514
bridge(5-5)H	1.211
bridge(5-5)S	0.861

(g)	ΔG_{H^*}
on-top(4)	0.019
on-top(5)	0.122
on-top(6)	0.872
bridge(4-4)	0.075
bridge(4-5)	0.215
bridge(5-5)	0.666

(h)	ΔG_{H^*}
on-top(4)	−0.103
on-top(5)	0.279
bridge(4-4)	−0.016
bridge(5-5)	1.226

(i)	ΔG_{H^*}
on-top	−1.98
bridge	−0.16
3-fold	0.583

FIG. 2. (a) The leftmost panel illustrates representative adsorption sites on borophene, including on-top(n) and threefold sites, where $n = 4$, 5, or 6 denotes the coordination number of the underlying boron atom (i.e., fourfold, fivefold, and sixfold coordinated sites, respectively). The second panel from the left schematically shows the out-of-plane distortion of the borophene surface upon hydrogen adsorption. The two rightmost panels depict the top and front views of the trigonal phase with H adsorbed at the on-top site; to ensure visual clarity, only the hexagonal ring directly beneath the adsorbed H atom is displayed on the front view. (b)–(e) depict the potential energy surface of single-H adsorption of the four borophene phases: (b) α, (c) β_{12}, (d) γ_3, and (e) trigonal. The H atom is moved within a specific region consisting of two adjacent triangular units as highlighted in (a). The distances between H and boron surface are fixed as 1.710, 1.712, 1.690, and 1.760 Å on the α, β_{12}, γ_3, and trigonal phases, respectively. The corresponding on-top site types at each vertex are also labeled in each panel. (f)–(i) depict the free energy diagrams for hydrogen adsorption on the α, β_{12}, γ_3, and trigonal phases, respectively. Each panel includes a table listing the calculated hydrogen adsorption free energy (ΔG_{H^*}) for the corresponding adsorption sites. In the table, "bridge(m–n)" denotes a bridge site located between two adjacent boron atoms with m- and n-fold coordination. The signs "bridge(5-5)H" and "bridge(5-5)S" in (b) refer to bridge sites located along the edges of hollow hexagons and hexagons containing an additional boron atom at the center, respectively.

phases, we select representative adsorption sites, including on-top, bridge, and threefold hollow sites, to evaluate their hydrogen evolution performance. These sites span different coordination environments and reflect the electronic diversity of each surface. In order to distinguish them, we assign labels based on their local coordination environment. Specifically, on-top sites located on fourfold, fivefold, and sixfold coordinated boron atoms are labeled as on-top(4), on-top(5), and on-top(6), respectively. Bridge sites are denoted as "bridge(m-n)", where m and n are the coordination numbers of adjacent atoms. Threefold site is located in the center of the triangle motif [shown in Fig. 2(a)]. For the trigonal phase, which exhibits a uniform arrangement of saturated boron atoms, only one unique site exists for each type, and no further distinction is necessary. The Gibbs free energy of hydrogen adsorption (ΔG_{H^*}) is utilized as a criterion to quantify the catalytic activity. Efficient HER catalysts require a good balance between hydrogen adsorption and desorption (hydrogen binds neither too weakly nor too strongly); hence, the reaction is considered optimal when the value of ΔG_{H^*} is close to zero [75]. We optimized each borophene surface again with a single hydrogen atom adsorbed by using the same computational conditions as for the freestanding structures. Local structural distortions are observed around the adsorption sites after relaxation, due to the release of adsorption-induced strain. Notably, the hydrogen atoms initially adsorbed at threefold sites tend to migrate to nearby on-top or bridge positions, indicating a more confined distribution of energetically favorable adsorption sites. The free energy diagrams of HER on the four borophene phases are depicted in Figs. 2(f)–2(i).

In general, an on-top site located on the low-coordination boron atom exhibits the optimal adsorption free energies. For example, the on-top(4) site (located on a fourfold coordinated boron atom) on β_{12} yields the lowest value of 0.019 eV in this phase. As the coordination number increases, the value of ΔG_{H^*} also rises. For instance, the on-top(5) site on the β_{12} phase exhibits a moderate adsorption free energy of 0.122 eV, while the on-top(6) site shows a much higher value of 0.872 eV, indicating reduced HER activity. Similar results can be found in both α and γ_3 phases. This trend is consistent with our previous analysis based on the PES images, where low-coordination sites generally present deeper potential wells. It is noteworthy that certain bridge sites, especially those spanning lower-coordinated atoms, also

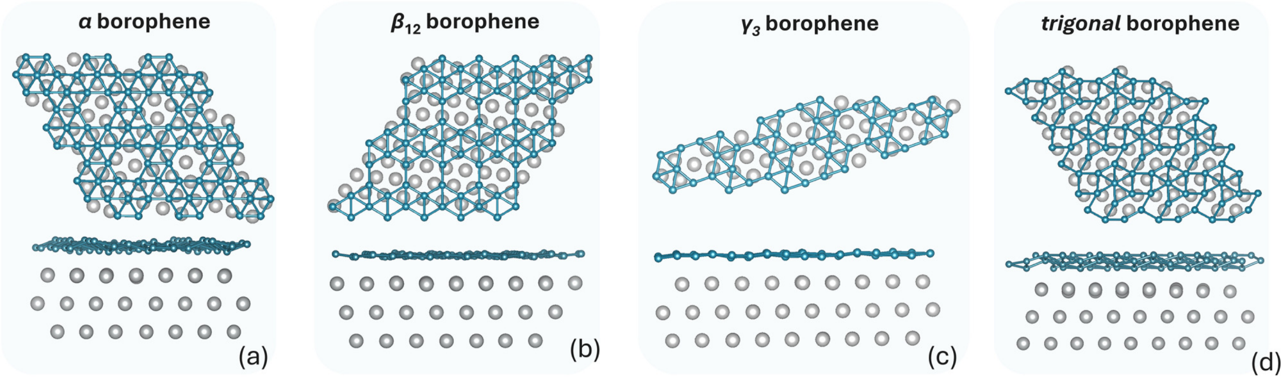

FIG. 3. Optimized structures of borophene phases on the Ag(111) substrate: (a) α, (b) β_{12}, (c) γ_3, and (d) trigonal phases. For each configuration, the upper panel shows the top view and the lower panel displays the side view, highlighting the interfacial interaction and structural deformation upon adsorption.

yield ΔG_{H^*} values comparable to on-top sites. On the γ_3 surface, the bridge(4-4) site exhibits a remarkably low value of -0.016 eV, which is the lowest value among all the selected sites on four phases. In contrast, the bridge(5-5) site shows a much higher value of 1.226 eV. As for the α phase, both bridge sites span two fivefold coordinated boron atoms. However, the one located at the edge of a hollow hexagon "bridge(5-5)H" exhibits a noticeably higher adsorption free energy compared to the one between two filled hexagons "bridge(5-5)S". Similar values can be found on the bridge(5-5)H site of β_{12} (0.666 eV) and the bridge(5-5)S site of γ_3 (1.226 eV). This can be attributed to the lower local charge density in this region, which weakens the interaction between the boron atoms and the adsorbed hydrogen.

Specifically, the trigonal structure exhibits a distinct behavior. The on-top site shows a significantly negative adsorption free energy of -1.980 eV, suggesting overly strong hydrogen binding that hinders desorption and thus reduces HER efficiency. It is noteworthy that the on-top(6) site in the α phase exhibits a similar trend ($\Delta G_{\mathrm{H}^*} = -0.514$). In principle, these B atoms are already highly saturated and should not easily form stable B-H bonds. The corresponding value of ΔG_{H^*} is expected to be positive as observed in the β_{12} phase. However, the α and trigonal phases have a lower concentration of hollow hexagons, making their structures more densely formed and causing stronger Pauli repulsion on the on-top(6) B atoms. When hydrogen adsorbs on this site, the B atom can be easily displaced out of the surface [as shown in Fig. 2(a)]. Eventually, it releases the internal lattice strain and forms a stronger H-B bond. Therefore, one sees more negative adsorption free energy in these phases. Meanwhile, the bridge and threefold sites yield values of -0.160 and 0.583 eV, respectively. These results suggest that the α, β_{12}, and γ_3 phases hold great promise for HER catalysis, whereas the trigonal phase is comparatively less effective.

C. Structures and stabilities of borophenes on a silver substrate

The calculations on the freestanding borophenes offer fundamental understanding of HER properties, while practical applications often involve interactions with supporting substrates. Considering that borophene phases are often experimentally synthesized on silver substrates [38,43,76], we utilize an Ag(111) surface to investigate how substrate interactions affect the structural and electronic properties of these systems. The Ag bulk lattice is reoptimized with the same computational parameters used for borophene. The optimized bulk lattice constant is 3.844 Å, corresponding to a in-plane constant of 2.718 Å. Each of the four aforementioned borophenes is placed on a three-layer Ag(111) slab with a lattice mismatch below 5%. The heterostructures are then geometrically optimized using the same computational parameters as for the freestanding borophenes. During the relaxation, the bottom two layers of the silver substrate are fixed to simulate bulk constraints, while the topmost layer in direct contact with borophene is allowed to fully relax. The resulting relaxed structures are shown in Fig. 3. The optimized vertical distances between the Ag(111) surface and the α, β_{12}, γ_3, and trigonal borophenes are 2.912, 2.410, 2.211, and 3.123 Å, respectively. The presence of the Ag substrate induces out-of-plane distortions in all cases. In particular, the trigonal structure undergoes significant reconstruction, which is not due to the highly saturated bonding environment of its boron atoms but rather to its densely packed bonding environment. Upon testing larger cells we found negligible changes in the geometry and adsorption energetics, confirming that the observed distortion is intrinsic and not a small-size artifact.

Unlike boron configurations with vacancies, which can locally adjust to release strain, the close-packed nature of the trigonal structure offers limited geometric flexibility, leading to substantial reconstruction under stress.

To quantify the interfacial interaction strength across different borophene phases, we compute the bonding energy per unit area (E_{bond}) as

$$E_{\mathrm{bond}} = \frac{E_{\mathrm{borophene/Ag}} - E_{\mathrm{Ag}} - E_{\mathrm{borophene}}^{\mathrm{supported}}}{A}, \tag{6}$$

where $E_{\mathrm{borophene/Ag}}$ is the total energy of the borophene/Ag(111) heterostructure, E_{Ag} is the total energy of the clean Ag slab, $E_{\mathrm{borophene}}^{\mathrm{supported}}$ is the free energy of the supported borophene layer in the heterostructure. The bonding energies for the four phases are -0.167 (α), -0.201 (β_{12}), -0.188 (γ_3), and -0.204 eV/Å^2 (trigonal), respectively. Among the four phases, the trigonal borophene exhibits the strongest interaction with the silver substrate, followed closely by

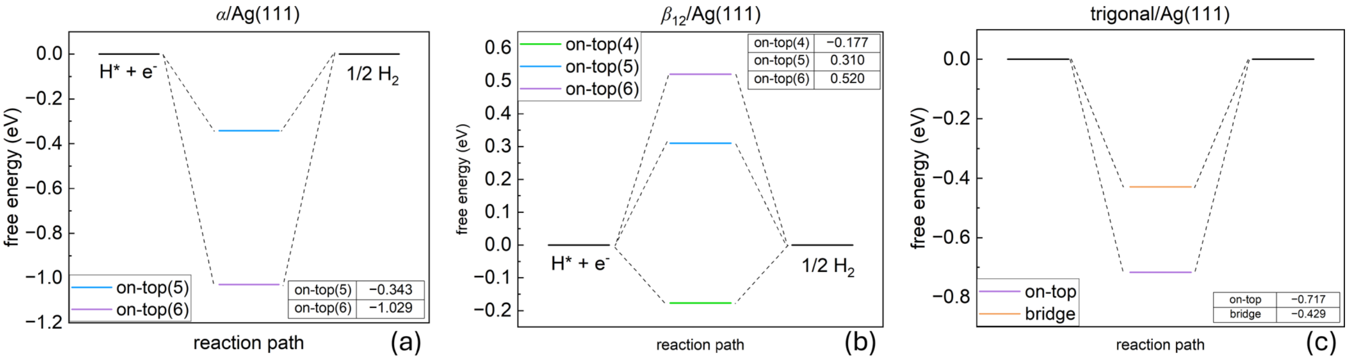

FIG. 4. Hydrogen adsorption free energy diagrams for (a) α, (b) β_{12}, and (c) trigonal borophene phases on the Ag(111) substrate. Each panel shows the calculated ΔG_{H^*} values at different adsorption sites, indicating the variation in hydrogen adsorption behavior across different borophene/Ag(111) interfaces.

β_{12} and γ_3, while the α phase shows the weakest interfacial bonding. In particular, the trigonal borophene initially features a highly saturated bonding environment around its boron atoms. Upon interaction with the Ag(111) substrate, it undergoes significant out-of-plane distortions, which help release internal stress within the borophene layer. These distortions also bring certain boron atoms closer to the silver surface (around 1.78 Å), thereby enhancing orbital overlap and strengthening the interfacial interaction. To evaluate the thermodynamic stability of supported borophene structures, we calculate the formation energy per boron atom using the following expression [77,78]:

$$E_{\text{form}} = \frac{E_{\text{borophene/Ag}} - E_{\text{Ag}} - N \times \mu_{\text{B}}}{A}, \tag{7}$$

where μ_{B} is the chemical potential of a single boron atom, typically taken from the energy per atom in the corresponding freestanding borophene phases. Interestingly, the lowest E_{form} is found on the trigonal phase with a negative value of -0.283 eV/Å^2, suggesting it is the most stable configuration on the Ag(111) surface. The β_{12} and γ_3 phases also show relatively high stability, consistent with their moderate interface bonding energies and preserved lattice structures. The α phase, which has the stablest freestanding configuration, has the highest formation energy (-0.164 eV/Å^2), indicating weaker overall thermodynamic favorability, consistent with its weaker bonding interaction with the Ag(111) surface.

D. HER performance of supported borophenes

Now we focus on the HER performance of the supported borophenes. Geometric optimizations for the heterostructures with a single H atom adsorbed on the borophene surface are performed. The initial adsorption sites are chosen in accordance with those selected in the freestanding scenarios. After relaxation, noticeable differences occur: in both the α and β_{12} structures, all the hydrogen atoms eventually relax to on-top sites. For the trigonal structure, both on-top and bridge sites remain stable after optimization, while the H atom initially located at the threefold site relaxes to an on-top site. As for the γ_3 phase, it undergoes significant structural disruption upon hydrogen adsorption, leading to a complete breakdown of its planar geometry, and is therefore excluded from the subsequent analysis. This indicates that it is in general not appropriate to transfer properties of free-standing layers to those of supported layers.

The corresponding Gibbs free energies for hydrogen adsorption on the supported α, β_{12}, and trigonal borophene structures are summarized in Fig. 4. In the freestanding case, sites with lower coordination tend to exhibit superior HER activity. This feature is preserved in the silver-supported structures. On the β_{12} phase, the most active site is the on-top(4) site with the lowest relative ΔG_{H^*} of -0.177 eV. For α, the most favorable one is the on-top(5) site ($\Delta G_{\text{H}^*} = -0.343$ eV). Importantly, compared to their freestanding counterparts, the absolute values of ΔG_{H^*} are increased in both α and β_{12}, indicating a reduced HER performance upon substrate support. A work function analysis is applied to evaluate the influence of the silver substrate support on the electronic properties of borophene. For the α phase, the work function increases from 3.986 to 4.342 eV upon interaction with the Ag(111) substrate. Based on a Bader charge analysis, this increase can be attributed to the combined effects of structural distortion and charge redistribution. Specifically, the strong interaction with the substrate induces a substantial out-of-plane distortion in the borophene lattice. This structural change facilitates the migration of electrons from the interface toward the vacuum surface, creating an inward surface dipole that effectively raises the energy barrier for electron emission. As shown in Fig. 5, within the borophene region, the electrostatic potential increases from approximately -32 eV in the freestanding structures to around -29 eV upon adsorption on the Ag(111) surface. Correspondingly, the vacuum level shifts from about 1.3 to 4.3 eV. The selected on-top(5) and on-top(6) sites are located on the outermost layer and gain 0.05e and 0.1 e from Ag substrate, respectively. This charge accumulation strengthens the B-H orbital hybridization and thus leads to a stronger H adsorption.

For the β_{12} phase, the work function decreases from 4.793 to 4.344 eV (Table II), indicating an enhanced ability of borophene to donate electrons to the 1s orbital of H. According to the Bader charge distribution analysis, both the on-top(4) and on-top(6) sites, which are located on the outermost layer, receive electrons (0.07 e and 0.2 e, respectively)

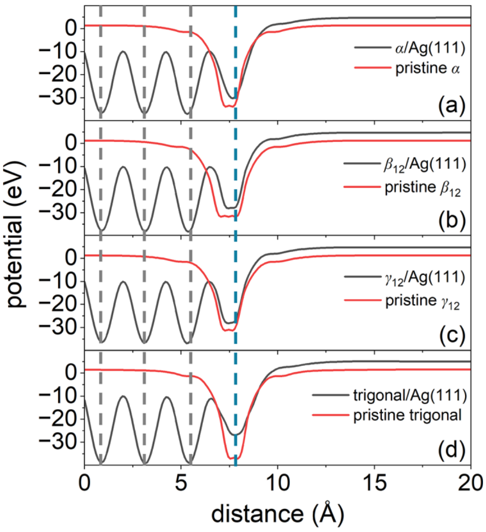

FIG. 5. Plane-averaged electrostatic potential along the z direction of borophene phases on the Ag(111) substrate: (a) α/Ag(111), (b) β_{12}/Ag(111), (c) γ_3/Ag(111), and (d) trigonal/Ag(111). The red and black lines denote the potential of the borophene/Ag and freestanding borophene structures, respectively. The dashed lines from left to right denote the positions of silver and boron layers.

from the Ag substrate. It effectively promotes the H-B bond and results in a more negative ΔG^*_{H}. As for the on-top(5) site, despite a minor charge increase of 0.01 e, it exhibits a more positive ΔG^*_{H}. This is attributed to the out-of-plane distortion which relocates the B atom into a structural "valley", making it more difficult to attract the H atom.

Similar to the α phase, the trigonal phase also exhibits a large increase in work function (from 3.098 to 4.747 eV) due to the substantial geometric distortion. Its bridge site exhibits a lower absolute value of ΔG_{H^*} compared to that on the freestanding surface [Fig. 4(c)]. Notably, the hydrogen adsorption free energy (ΔG^*_{H}) of the on-top site increases from −1.980 to −0.717 eV, indicating a weakened B-H interaction upon introducing the Ag support. As we mentioned in the previous section, in the freestanding state, the B atom undergoes a large out-of-plane displacement toward the H atom due to Pauli repulsion, resulting in a very strong B-H bond. However, in the supported system, the Ag substrate induces a significant distortion on borophene and effectively reduces the structural strain. In this case, the B atom remains bonded to the borophene. This restriction decreases the overlap between B and H orbitals, thereby increasing the adsorption free energy. In summary, the presence of the Ag(111) substrate generally suppresses the HER performance across the α, β_{12}, and trigonal phases of borophene.

TABLE II. Summary of structural and electronic properties of borophene/Ag(111) heterostructures. d denotes the vertical distance between the borophene layer and Ag(111) surface; E_{bond} denotes average interfacial bonding energy per unit area; E_{form} is the formation energy per boron atom; Φ denotes the work function of the heterostructure. Values in parentheses indicate the work function of the corresponding freestanding borophene sheets.

Phases	d (Å)	E_{bond} (eV/Å^2)	E_{form} (eV/Å^2)	Φ (eV)
α/Ag	2.912	−0.167	−0.164	4.342 (3.986)
β_{12}/Ag	2.410	−0.201	−0.202	4.344 (4.793)
γ_3/Ag	2.211	−0.188	−0.181	4.279 (4.681)
Trigonal/Ag	3.123	−0.204	−0.283	4.747 (3.098)

Finally, we like to discuss whether our results are also of significance for other metal substrates such as, e.g., Cu or Al. The key factors determining the interaction between borophene and a substrate include charge transfer, work function difference, and the strength of metal-boron bonding. Ag(111) induces a significant electronic perturbation and charge redistribution in borophene, which in our calculations leads to suppressed intrinsic HER activity for certain adsorption sites. However, for substrates with higher work function [such as Au(111)], charge transfer may be reduced, potentially preserving more of the pristine borophene electronic character, and therefore preserve the high HER activity. For substrates with stronger chemical interactions (such as Cu or Al), more pronounced hybridization with borophene may occur, which could either enhance or disrupt the active sites depending on the degree of charge reorganization and surface reconstruction. Such substrate dependence has been discussed in several related two-dimensional materials studies, where different substrates lead to varying degrees of charge transfer and adsorption strength [79,80]. Therefore, although our present results show that Ag(111) tends to suppress the HER activity in borophene, the broader influence on other substrates remains open, which would require further dedicated investigations.

IV. CONCLUSIONS

In this work, we systematically studied the hydrogen evolution reaction performance of four borophene phases using first-principles calculations, including α, γ_3, β_{12}, and trigonal phases. We found that in the freestanding monolayer surfaces, low-coordinated boron sites generally exhibit more favorable hydrogen adsorption, with the α, β_{12}, and γ_3 phases showing promising catalytic performance. In contrast, the trigonal phase performs poorly due to its highly coordinated, saturated bonding environment. When supported on an Ag(111) surface, the borophene structures undergo substrate-induced distortions, which tend to reduce HER activity by weakening adsorption strength. Although the coordination-dependent trend is largely preserved and some sites on the supported layers still exhibit moderate activity, this result clearly indicates that a metal support can have a significant influence on the properties of two-dimensional layers. These findings clarify the crucial role of local atomic coordination in governing hydrogen adsorption energetics and HER catalytic activity in borophene. Moreover, the study highlights the significant impact of substrate interactions, which can both modulate structural stability and electronic properties, thereby influencing catalytic behavior. Understanding these effects provides valuable insight for the rational design and optimization of boron-based catalysts.

ACKNOWLEDGMENTS

The authors are grateful for financial support through the Bundesministerium für Wirtschaft und Klimaschutz (BMWK) project AQUAS (Grant No. 01MQ22003C) and the Dr. Barbara-Mez-Starck foundation. Furthermore, computer time provided by the state of Baden-Württemberg through bwHPC and the German Research Foundation (DFG) through Grant No. INST 40/575-1 FUGG (JUSTUS 2 cluster) are gratefully acknowledged.

DATA AVAILABILITY

The data that support the findings of this article are openly available [81], embargo periods may apply.

[1] D. Deng, K. Novoselov, Q. Fu, N. Zheng, Z. Tian, and X. Bao, Catalysis with two-dimensional materials and their heterostructures, Nat. Nanotechnol. **11**, 218 (2016).

[2] L. Tang, X. Meng, D. Deng, and X. Bao, Confinement catalysis with 2D materials for energy conversion, Adv. Mater. **31**, 1901996 (2019).

[3] L. Zhao, B. Wang, and R. Wang, A critical review on new and efficient 2D materials for catalysis, Adv. Mater. Interfaces **9**, 2200771 (2022).

[4] A. K. Katiyar, A. T. Hoang, D. Xu, J. Hong, B. J. Kim, S. Ji, and J.-H. Ahn, 2D materials in flexible electronics: Recent advances and future prospectives, Chem. Rev. **124**, 318 (2024).

[5] E. C. Ahn, 2D materials for spintronic devices, npj 2D Mater. Appl. **4**, 17 (2020).

[6] A. Groß, Adsorption at nanostructured surfaces from first principles, J. Comput. Theor. Nanosci. **5**, 894 (2008).

[7] J. López-Andarias, A. Bauzá, N. Sakai, A. Frontera, and S. Matile, Remote control of anion–π catalysis on fullerene-centered catalytic triads, Angew. Chem. Int. Ed. **130**, 11049 (2018).

[8] Y. Pan, X. Liu, W. Zhang, Z. Liu, G. Zeng, B. Shao, Q. Liang, Q. He, X. Yuan, D. Huang, *et al.*, Advances in photocatalysis based on fullerene C_{60} and its derivatives: Properties, mechanism, synthesis, and applications, Appl. Catal. B **265**, 118579 (2020).

[9] S. J. Hong, H. Chun, M. Hong, and B. Han, N- and B-doped fullerene as peroxidase-and catalase-like metal-free nanozymes with pH-switchable catalytic activity: A first-principles approach, Appl. Surf. Sci. **598**, 153715 (2022).

[10] X. Chang, Y. Xu, and M. von Delius, Recent advances in supramolecular fullerene chemistry, Chem. Soc. Rev. **53**, 47 (2024).

[11] A. S. Brady-Estevez, S. Kang, and M. Elimelech, Carbon nanotubes, Small **4**, 481 (2008).

[12] P. Serp and E. Castillejos, Catalysis in carbon nanotubes, ChemCatChem **2**, 41 (2010).

[13] M. F. De Volder, S. H. Tawfick, R. H. Baughman, and A. J. Hart, Carbon nanotubes: Present and future commercial applications, Science **339**, 535 (2013).

[14] A. K. Geim, Graphene: Status and prospects, Science **324**, 1530 (2009).

[15] Y. Li, H. Wang, L. Xie, Y. Liang, G. Hong, and H. Dai, MoS_2 nanoparticles grown on graphene: An advanced catalyst for the hydrogen evolution reaction, J. Am. Chem. Soc. **133**, 7296 (2011).

[16] H.-J. Qiu, Y. Ito, W. Cong, Y. Tan, P. Liu, A. Hirata, T. Fujita, Z. Tang, and M. Chen, Nanoporous graphene with single-atom nickel dopants: An efficient and stable catalyst for electrochemical hydrogen production, Angew. Chem. Int. Ed. **54**, 14031 (2015).

[17] Y. Jiao, Y. Zheng, K. Davey, and S.-Z. Qiao, Activity origin and catalyst design principles for electrocatalytic hydrogen evolution on heteroatom-doped graphene, Nat. Energy **1**, 16130 (2016).

[18] X. Li, J. Yu, S. Wageh, A. A. Al-Ghamdi, and J. Xie, Graphene in photocatalysis: A review, Small **12**, 6640 (2016).

[19] C. Lee, X. Wei, J. W. Kysar, and J. Hone, Measurement of the elastic properties and intrinsic strength of monolayer graphene, Science **321**, 385 (2008).

[20] A. H. Castro Neto, F. Guinea, N. M. R. Peres, K. S. Novoselov, and A. K. Geim, The electronic properties of graphene, Rev. Mod. Phys. **81**, 109 (2009).

[21] C. Soldano, A. Mahmood, and E. Dujardin, Production, properties and potential of graphene, Carbon **48**, 2127 (2010).

[22] A. Olabi, M. A. Abdelkareem, T. Wilberforce, and E. T. Sayed, Application of graphene in energy storage device – A review, Renew. Sustain. Energy Rev. **135**, 110026 (2021).

[23] Y. Qi, L. Sun, and Z. Liu, Super graphene-skinned materials: An innovative strategy toward graphene applications, ACS Nano **18**, 4617 (2024).

[24] H. Gao, Z. Wang, J. Cao, Y. C. Lin, and X. Ling, Advancing nanoelectronics applications: Progress in non-van der Waals 2D materials, ACS Nano **18**, 16343 (2024).

[25] J. Zhao, P. Ji, Y. Li, R. Li, K. Zhang, H. Tian, K. Yu, B. Bian, L. Hao, X. Xiao, *et al.*, Ultrahigh-mobility semiconducting epitaxial graphene on silicon carbide, Nature (London) **625**, 60 (2024).

[26] J. Azizi, A. Groß, and H. Euchner, Computational investigation of carbon based anode materials for Li- and post-Li- ion batteries, ChemSusChem **17**, e202301493 (2024).

[27] H.-J. Zhai, B. Kiran, J. Li, and L.-S. Wang, Hydrocarbon analogues of boron clusters—planarity, aromaticity and antiaromaticity, Nat. Mater. **2**, 827 (2003).

[28] N. Gonzalez Szwacki, A. Sadrzadeh, and B. I. Yakobson, B_{80} fullerene: An *ab initio* prediction of geometry, stability, and electronic structure, Phys. Rev. Lett. **98**, 166804 (2007).

[29] W. Huang, A. P. Sergeeva, H.-J. Zhai, B. B. Averkiev, L.-S. Wang, and A. I. Boldyrev, A concentric planar doubly π-aromatic B_{19}^- cluster, Nat. Chem. **2**, 202 (2010).

[30] H.-J. Zhai, Y.-F. Zhao, W.-L. Li, Q. Chen, H. Bai, H.-S. Hu, Z. A. Piazza, W.-J. Tian, H.-G. Lu, Y.-B. Wu, Y.-W. Mu, G.-F. Wei, Z.-P. Liu, J. Li, S.-D. Li, and L.-S. Wang, Observation of an all-boron fullerene, Nat. Chem. **6**, 727 (2014).

[31] B. Kiran, S. Bulusu, H.-J. Zhai, S. Yoo, X. C. Zeng, and L.-S. Wang, Planar-to-tubular structural transition in boron clusters: B_{20} as the embryo of single-walled boron nanotubes, Proc. Natl. Acad. Sci. USA **102**, 961 (2005).

[32] K. C. Lau, R. Orlando, and R. Pandey, First-principles study of crystalline bundles of single-walled boron nanotubes

with small diameter, J. Phys.: Condens. Matter **20**, 125202 (2008).

[33] F. Liu, C. Shen, Z. Su, X. Ding, S. Deng, J. Chen, N. Xu, and H. Gao, Metal-like single crystalline boron nanotubes: Synthesis and *in situ* study on electric transport and field emission properties, J. Mater. Chem. **20**, 2197 (2010).

[34] X. Wu, J. Dai, Y. Zhao, Z. Zhuo, J. Yang, and X. C. Zeng, Two-dimensional boron monolayer sheets, ACS Nano **6**, 7443 (2012).

[35] B. Feng, J. Zhang, Q. Zhong, W. Li, S. Li, H. Li, P. Cheng, S. Meng, L. Chen, and K. Wu, Experimental realization of two-dimensional boron sheets, Nat. Chem. **8**, 563 (2016).

[36] Z. Wu, G. Tai, W. Shao, R. Wang, and C. Hou, Experimental realization of quasicubic boron sheets, Nanoscale **12**, 3787 (2020).

[37] Z. A. Piazza, H.-S. Hu, W.-L. Li, Y.-F. Zhao, J. Li, and L.-S. Wang, Planar hexagonal B_{36} as a potential basis for extended single-atom layer boron sheets, Nat. Commun. **5**, 3113 (2014).

[38] D. Li, J. Gao, P. Cheng, J. He, Y. Yin, Y. Hu, L. Chen, Y. Cheng, and J. Zhao, 2D boron sheets: Structure, growth, and electronic and thermal transport properties, Adv. Funct. Mater. **30**, 1904349 (2020).

[39] B. Kiraly, X. Liu, L. Wang, Z. Zhang, A. J. Mannix, B. L. Fisher, B. I. Yakobson, M. C. Hersam, and N. P. Guisinger, Borophene synthesis on Au(111), ACS Nano **13**, 3816 (2019).

[40] W. Li, L. Kong, C. Chen, J. Gou, S. Sheng, W. Zhang, H. Li, L. Chen, P. Cheng, and K. Wu, Experimental realization of honeycomb borophene, Sci. Bull. **63**, 282 (2018).

[41] R. Wu, I. K. Drozdov, S. Eltinge, P. Zahl, S. Ismail-Beigi, I. Božović, and A. Gozar, Large-area single-crystal sheets of borophene on Cu(111) surfaces, Nat. Nanotechnol. **14**, 44 (2019).

[42] J.-Y. Chung, Y. Yuan, T. P. Mishra, C. Joseph, P. Canepa, P. Ranjan, E. H. S. Sadki, S. Gradečak, and S. Garaj, Structure and exfoliation mechanism of two-dimensional boron nanosheets, Nat. Commun. **15**, 6122 (2024).

[43] Q. Zhong, L. Kong, J. Gou, W. Li, S. Sheng, S. Yang, P. Cheng, H. Li, K. Wu, and L. Chen, Synthesis of borophene nanoribbons on Ag(110) surface, Phys. Rev. Mater. **1**, 021001 (2017).

[44] B. Feng, O. Sugino, R.-Y. Liu, J. Zhang, R. Yukawa, M. Kawamura, T. Iimori, H. Kim, Y. Hasegawa, H. Li, L. Chen, K. Wu, H. Kumigashira, F. Komori, T.-C. Chiang, S. Meng, and I. Matsuda, Dirac fermions in borophene, Phys. Rev. Lett. **118**, 096401 (2017).

[45] X. Liu, Z. Wei, I. Balla, A. J. Mannix, N. P. Guisinger, E. Luijten, and M. C. Hersam, Self-assembly of electronically abrupt borophene/organic lateral heterostructures, Sci. Adv. **3**, e1602356 (2017).

[46] X. Liu, Z. Zhang, L. Wang, B. I. Yakobson, and M. C. Hersam, Intermixing and periodic self-assembly of borophene line defects, Nat. Mater. **17**, 783 (2018).

[47] X. Liu and M. C. Hersam, Borophene-graphene heterostructures, Sci. Adv. **5**, eaax6444 (2019).

[48] N. A. Vinogradov, A. Lyalin, T. Taketsugu, A. S. Vinogradov, and A. Preobrajenski, Single-phase borophene on Ir(111): Formation, structure, and decoupling from the support, ACS Nano **13**, 14511 (2019).

[49] Y. Wang, L. Kong, C. Chen, P. Cheng, B. Feng, K. Wu, and L. Chen, Realization of regular-mixed quasi-1D borophene chains with long-range order, Adv. Mater. **32**, 2005128 (2020).

[50] X.-F. Zhou, X. Dong, A. R. Oganov, Q. Zhu, Y. Tian, and H.-T. Wang, Semimetallic two-dimensional boron allotrope with massless Dirac fermions, Phys. Rev. Lett. **112**, 085502 (2014).

[51] B. Feng, J. Zhang, R.-Y. Liu, T. Iimori, C. Lian, H. Li, L. Chen, K. Wu, S. Meng, F. Komori, and I. Matsuda, Direct evidence of metallic bands in a monolayer boron sheet, Phys. Rev. B **94**, 041408 (2016).

[52] L. Adamska, S. Sadasivam, J. J. I. Foley, P. Darancet, and S. Sharifzadeh, First-principles investigation of borophene as a monolayer transparent conductor, J. Phys. Chem. C **122**, 4037 (2018).

[53] Y. An, J. Jiao, Y. Hou, H. Wang, D. Wu, T. Wang, Z. Fu, G. Xu, and R. Wu, How does the electric current propagate through fully-hydrogenated borophene, Phys. Chem. Chem. Phys. **20**, 21552 (2018).

[54] S. H. Mir, S. Chakraborty, P. C. Jha, J. Wärnå, H. Soni, P. K. Jha, and R. Ahuja, Two-dimensional boron: Lightest catalyst for hydrogen and oxygen evolution reaction, Appl. Phys. Lett. **109**, 053903 (2016).

[55] Y. Chen, G. Yu, W. Chen, Y. Liu, G.-D. Li, P. Zhu, Q. Tao, Q. Li, J. Liu, X. Shen, H. Li, X. Huang, D. Wang, T. Asefa, and X. Zou, Highly active, nonprecious electrocatalyst comprising borophene subunits for the hydrogen evolution reaction, J. Am. Chem. Soc. **139**, 12370 (2017).

[56] L. Shi, C. Ling, Y. Ouyang, and J. Wang, High intrinsic catalytic activity of two-dimensional boron monolayers for the hydrogen evolution reaction, Nanoscale **9**, 533 (2017).

[57] Y. Singh, S. Back, and Y. Jung, Computational exploration of borophane-supported single transition metal atoms as potential oxygen reduction and evolution electrocatalysts, Phys. Chem. Chem. Phys. **20**, 21095 (2018).

[58] M. Xu, R. Wang, K. Bian, C. Hou, Y. Wu, and G. Tai, Triclinic boron nanosheets high-efficient electrocatalysts for water splitting, Nanotechnol. **33**, 075601 (2022).

[59] X. Wang, R. Wu, P. Tian, Y. Yan, Y. Gao, and F. Xuan, Borophene nanoribbons via strain engineering for the hydrogen evolution reaction: A first-principles study, J. Phys. Chem. C **125**, 16955 (2021).

[60] S. Sakong, D. Mahlberg, T. Roman, M. Pandey, and A. Groß, Influence of local inhomogenities and the electrochemical environment on the oxygen reduction reaction on Pt-based electrodes: A DFT study, J. Phys. Chem. C **124**, 27604 (2020).

[61] X. Zou and Y. Zhang, Noble metal-free hydrogen evolution catalysts for water splitting, Chem. Soc. Rev. **44**, 5148 (2015).

[62] J. N. Hansen, H. Prats, K. K. Toudahl, N. Mørch Secher, K. Chan, J. Kibsgaard, and I. Chorkendorff, Is there anything better than Pt for HER, ACS Energy Lett. **6**, 1175 (2021).

[63] G. Kresse and J. Furthmüller, Efficiency of *ab-initio* total energy calculations for metals and semiconductors using a plane-wave basis set, Comp. Mater. Sci. **6**, 15 (1996).

[64] G. Kresse and D. Joubert, From ultrasoft pseudopotentials to the projector augmented-wave method, Phys. Rev. B **59**, 1758 (1999).

[65] P. E. Blöchl, Projector augmented-wave method, Phys. Rev. B **50**, 17953 (1994).

[66] B. Hammer, L. B. Hansen, and J. K. Nørskov, Improved adsorption energetics within density-functional theory using revised Perdew-Burke-Ernzerhof functionals, Phys. Rev. B **59**, 7413 (1999).

[67] J. P. Perdew, K. Burke, and M. Ernzerhof, Generalized gradient approximation made simple, Phys. Rev. Lett. **77**, 3865 (1996).

[68] S. Grimme, S. Ehrlich, and L. Goerigk, Effect of the damping function in dispersion corrected density functional theory, J. Comp. Chem. **32**, 1456 (2011).

[69] D. Mahlberg, S. Sakong, K. Forster-Tonigold, and A. Groß, Improved DFT adsorption energies with semiempirical dispersion corrections, J. Chem. Theory Comput. **15**, 3250 (2019).

[70] V. Wang, N. Xu, J.-C. Liu, G. Tang, and W.-T. Geng, VASPKIT: A user-friendly interface facilitating high-throughput computing and analysis using VASP code, Comp. Phys. Commun. **267**, 108033 (2021).

[71] K. Krischer and E. R. Savinova, Electrochemical catalysis, in *Handbook of Heterogeneous Catalysis*, edited by G. Ertl, H. Knözinger, F. Schüth, and J. Weitkamp (Wiley-VCH, Chichester, UK, 2009), pp. 1873–1905.

[72] J. K. Nørskov, T. Bligaard, A. Logadottir, J. R. Kitchin, J. G. Chen, S. Pandelov, and U. Stimming, Trends in the exchange current for hydrogen evolution, J. Electrochem. Soc. **152**, J23 (2005).

[73] P. K. Schmidt, K. Christmann, G. Kresse, J. Hafner, M. Lischka, and A. Groß, Coexistence of atomic and molecular chemisorption states: H_2/Pd(210), Phys. Rev. Lett. **87**, 096103 (2001).

[74] A. Groß, A. Eichler, J. Hafner, M. J. Mehl, and D. A. Papaconstantopoulos, Unified picture of the molecular adsorption process: O_2/Pt(111), Surf. Sci. **539**, L542 (2003).

[75] J. K. Nørskov, J. Rossmeisl, A. Logadottir, L. Lindqvist, J. R. Kitchin, T. Bligaard, and H. Jónsson, Origin of the overpotential for oxygen reduction at a fuel-cell cathode, J. Phys. Chem. B **108**, 17886 (2004).

[76] C. Hou, G. Tai, Y. Liu, Z. Wu, X. Liang, and X. Liu, Borophene-based materials for energy, sensors and information storage applications, Nano Res. Energy **2**, e9120051 (2023).

[77] F. Gossenberger, F. Juarez, and A. Groß, Sulfate, bisulfate, and hydrogen co-adsorption on Pt(111) and Au(111) in an electrochemical environment, Front. Chem. **8**, 634 (2020).

[78] A. Groß, Reversible vs standard hydrogen electrode scale in interfacial electrochemistry from a theoretician's atomistic point of view, J. Phys. Chem. C **126**, 11439 (2022).

[79] S. Lee, B. Min, and J. Bang, Substrate effect on hydrogen evolution reaction in two-dimensional Mo_2C monolayers, Sci. Rep. **12**, 6076 (2022).

[80] A. Jagminas, A. Naujokaitis, P. Gaigalas, S. Ramanavicius, M. Kurtinaitiene, and R. Trusovas, Substrate impact on the structure and electrocatalyst properties of molybdenum disulfide for HER from water, Metals **10**, 1251 (2020).

[81] NOMAD, https://dx.doi.org/10.17172/NOMAD/2025.10.14-1.